Numerical investigation of case hardening of plant tissue during dying and its influence on the cellular level shrinkage

H.C.P. Karunasena,[1,2] **Y.T. Gu,**[1] **R.J. Brown**[1] **and W. Senadeera** *[1]

Abstract

Dried plant food materials are one of the major contributors to the global food industry. Widening the fundamental understanding on different mechanisms of food material alterations during drying assists the development of novel dried food products and processing techniques. In this regard, case hardening is an important phenomenon, commonly observed during the drying processes of plant food materials, which significantly influences the product quality and process performance. In this work, a recent meshfree-based numerical model of the authors is further improved and used to simulate the influence of case hardening on shrinkage characteristics of plant tissues during drying. In order to model fluid and wall mechanisms in each cell, Smoothed Particle Hydrodynamics (SPH) and the Discrete Element Method (DEM) are used. The model is fundamentally more capable of simulating large deformation of multiphase materials, when compared with conventional grid-based modelling techniques such as Finite Element Methods (FEM) or Finite Difference Methods (FDM). Case hardening is implemented by maintaining distinct moisture levels in the different cell layers of a given tissue. In order to compare and investigate different factors influencing tissue deformations under case hardening, four different plant tissue varieties (apple, potato, carrot and grape) are studied. The simulation results indicate that the inner cells of any given tissue undergo limited shrinkage and cell wall wrinkling compared to the case hardened outer cell layers of the tissues. When comparing unique deformation characteristics of the different tissues, irrespective of the normalised moisture content, the cell size, cell fluid turgor pressure and cell wall characteristics influence the tissue response to case hardening.

Keywords: Food drying; Case hardening; Shrinkage; Plant tissue; Numerical modelling; Meshfree methods; SPH; DEM; Microscale models;

[1] *School of Chemistry, Physics and Mechanical Engineering, Faculty of Science and Engineering, Queensland University of Technology, 2-George Street, Brisbane,QLD 4001, Australia. Fax: +61 7 31381469; Tel: +61 7 31381009; E-mail:w3.senadeera@qut.edu.au (Wijitha Senadeera)*

[2] *Department of Mechanical and Manufacturing Engineering, Faculty of Engineering, University of Ruhuna, Hapugala, Galle, Sri Lanka. E-mail: chaminda@mme.ruh.ac.lk (H.C.P. Karunasena)*

1. Introduction

Global demand for food materials is ever increasing. As living standards improve, plant-based food materials are becoming more popular. In this regard, the contribution of dried food products is of higher importance to the food supply chain, as well as the economy. Currently, drying is used on about 20% of the world's perishable crops, and is a key food processing technique [1]. Due to the high moisture content of plant food materials, which can even be as high as 90% by weight [2], these are frequently subjected to microbial spoilage. In this regard, drying helps to preserve the food material by reducing the moisture content, which is achieved through various drying techniques [3]. Due to the moisture reduction, the food structure undergoes critical deformations both in the microscale and the macroscale, leading to multi-scale shrinkage phenomena [4-11]. Shrinkage is mainly influenced by the moisture content of the food material [4-8, 12-14], drying temperature [14-17] and cell turgor pressure [18]. Researchers have frequently conducted studies on food material shrinkage, leading to different empirical [19] and theoretical models [20, 21]. However, only a limited number of numerical models are available for food material deformations during drying. These models are frequently based on grid-based modelling techniques such as Finite Element Methods (FEM) and Finite Difference Methods (FDM), and have clear limitations in handling non-continuum multiphasic materials, under excessive deformation and phase change conditions [22]. For instance, an FEM-based gel material model [23] and an FEM-based plant leaf drying model [24] are examples of the macroscale models, which have clear application limitations due to their grid-based nature [25]. In the case of the microscale studies, there are several models developed for basic micromechanical behavioural studies of fresh cells and tissues [20, 26-31]. Particularly for cellular drying studies, an FEM-based tissue model is reported which couples water transport phenomena with cell deformations [32]. The model can only simulate a limited moisture content reduction (30%) and is not capable of accounting for cell wall wrinkling during drying. All these examples imply the limitations of grid-based modelling techniques for the simulation of plant food material shrinkage during drying.

As an alternative, meshfree methods are fundamentally more appropriate for simulation of multiphase systems with large deformations, as these methods basically do not involve any interconnected grids during the discretisation process [22, 33]. In the case of food material microstructure, there are some meshfree-based research works reported, which basically focus on fresh cells and tissues [34-36]. Recently, this approach was further improved by accounting for distinct mechanisms of cellular level drying of plant food materials, and 2-D models were developed for dry plant cells [37-40] and tissues [25, 41], in order to study cellular deformations during drying. The approach basically approximates a tissue as an aggregate of cells, where each cell consists of two components: cell fluid and cell wall. The cell fluid is approximated to a Newtonian fluid and modelled with Smoothed Particle Hydrodynamics (SPH), which is a popular particle-based meshfree method [22, 42]. The cell wall is

approximated to a moist solid boundary and modelled with Discrete Element Method (DEM). Both SPH and DEM use particles for discretisation of the domains. As the cell evolves with time, fluid and wall particles move according to the different force interactions defined to account for distinct cellular drying mechanisms such as: cell moisture reduction, turgor loss, cell wall drying and contractions, cell wall bending resistance, fluid-wall attractive interactions and intercellular interactions. Compared to the conventional grid-based techniques, this novel meshfree-based modelling approach is observed to be more appropriate for modelling the cellular structural deformations of plant food materials during drying, particularly when simulating extensive moisture content reduction, cell wall wrinkling and shrinkage [25, 41].

In almost all the tissue drying numerical models developed so far [25, 32, 41], the tissue is assumed to undergo uniform drying, where all the cells in the tissue are subjected to similar drying conditions. However, in actual drying processes, when bigger tissues with large numbers of cells are involved, case hardening is a phenomenon frequently observed. It causes the outer cell layers of a given tissue to undergo excessive drying, which eventually becomes a hardened case that resists further moisture removal from the interior cell layers. Under extensive drying, the hardened case can even become cracked, while the interior cell layers are still quite wet [2, 15, 43, 44]. With this background, the case hardening phenomenon is of great significance to the food industry, particularly with respective to product quality and process performance. Therefore, in order to establish a better understanding of the case hardening phenomenon, a dedicated numerical model is needed, which is the main focus of this work. By improving on a recent meshfree-based tissue drying model developed by the authors [25], the case hardening is incorporated into the tissue model by implementing different moist cell layers in a given tissue, corresponding with the dry tissue state of interest. Additionally, the effect of case hardening is studied on different plant tissues having distinct morphological characteristics based on cell size, wall thickness, cell wall stiffness, cell wall contractions, turgor pressure, and pectin layer dimensions and stiffness. Accordingly, apple, potato, carrot and grape tissues were selected for the study, considering the significance to the food drying industry and the availability of experimental results for comparison and validation of the model predictions.

Since the model development in this study is based on a recent tissue model of the authors, the main body of the paper is dedicated to introducing novel developments, result presentations, discussions and conclusions. All other additional modelling details and fundamental formulations are included in the Appendix A.

2. Model Development

2.1. Basic concepts of modelling a plant tissue

For the simulations of this work, a pre-existing meshfree-based 2-D tissue model is used [25], which was developed after a series of studies, beginning with a single cell [37-40] and progressing to a basic tissue [25, 41, 45]. As presented in Fig. 1, a plant tissue is approximated to an aggregation of cylindrical cells, each filled with cell fluid, surrounded by a flexible cell wall. To facilitate 2-D study, the cell is assumed to undergo uniform radial deformations along the cylindrical axis, and the top surface of each cell is referred to as the 2-D model, representing cellular mechanisms of the whole cell. The cell fluid is modelled with Smoothed Particle Hydrodynamics (SPH), a popular meshfree method applicable to hydrodynamic problems, and the cell wall is modelled with Discrete Element Method (DEM). Both cell fluid and cell wall are treated as individual sets of particles during the domain discretisation [37, 38]. The cell wall is approximated to a visco-elastic solid boundary and a Neo-Hookean solid material approximation is used along with a supplementary viscous term [34, 35]. Accordingly, as presented in Fig. 2, the cell wall is modelled as particles connected with different force interactions such as stiff, damping, repulsive, attractive, bending and contraction, in order to account for the basic mechanisms existing in realistic plant cell walls, and to model their response during drying [37] (see Section 8.1 of Appendix A for details). Cell fluid is approximated to a Newtonian fluid with low-Reynolds number flow characteristics, and modelled with the use of pressure, viscous, repulsion and attraction force interactions, as presented in Fig. 3. [37] (see Section 8.2 of Appendix A for details). As illustrated in Fig. 4, the above single cell model is initiated as a hexagon and such cells are bonded together by stiff contacts along with a repulsive contact, according to the methodology proposed in a previous work [25] (see Section 8.3 of Appendix A for details). The resulting cellular configuration replicates the honeycomb-shaped cellular structure, commonly observed in plant tissues and the pectin layer existing in between the actual cells of such tissues. Accordingly, a square shaped tissue was modelled by aggregating 23 hexagonal cells and cellular properties were set in each case, according to the tissue variety used (see Section 2.2 for details).

2.2. Setting up the particle scheme for the model

The simulations were conducted on tissues of four plant food types, which are of high industrial interest: apple, potato, carrot and grape. Table 1 presents the customised physical properties used for each of the plant materials and Table 2 presents the other model parameters commonly used for modelling. In each case, when setting up the particle scheme for each cell in the tissue models, wall particles are firstly placed on a hexagon, equally spaced. The hexagon size is determined such that its perimeter is equal to the perimeter of a fresh cell of the plant material of interest. The fluid particles are placed inside the wall boundary in a square arrangement such that the initial inter-particle gap of

the fluid particles is equal to the initial gap between the wall particles. Considering the model consistency and computational cost, a moderate particle resolution is used for the simulations such that 96 wall particles and 656 fluid particles are involved [25]. The model is time-evolved using the Leapfrog time integrator [22], with a sufficiently small time step defined by the Courant-Friedrichs-Lewy (CFL) criteria [22, 46]. Also, in order to improve model stability by preventing fluid particle penetrations through the cell wall, a set of zero-mass virtual particles are used which are placed in between the cell wall particles [35, 38].

2.3. Simulation of plant tissue drying (without case hardening)

For tissues without case hardening, each cell in the tissue is equally set and allowed to undergo a similar time-evolution sequence. In the case of fresh tissue, each cell is setup by initiating the mass of the cell fluid and wall particles, and time-evolved by using the corresponding turgor pressure and osmotic potential values, thereby, replicating real cells which have semipermeable cell walls. The cell fluid mass (i.e. mass of each fluid particle) tends to fluctuate until the turgor pressure and the magnitude of the osmotic potential become equal according to the Eq. (A.18). Such fluid particle mass fluctuations result in fluid density fluctuation as defined by Eq. (A.14), which eventually cause sudden turgor pressure fluctuations as defined by Eq. (A.13). These turgor pressure fluctuations cause the cell wall to displace, leading to different states of cellular deformations. As a result, the turgor pressure fluctuates again, and it leads to secondary cell fluid mass fluctuations defined by Eq. (A.18). In the meantime, the cell wall mass is kept fixed at the initially set value, corresponding to the particular dryness state. This cycle of model evolution repeats until the cell turgor pressure becomes almost equal to the magnitude of the osmotic potential. At the end of simulations, the steady state cell particle arrangement is referred to as the fresh cell state and the cell moisture content and other geometrical properties are computed to characterise the fresh cell state for analysis purposes (see Section 3 for details).

Dried tissues without case hardening are also similarly simulated and each cell in the tissue is initiated with identical model parameters and is time-evolved. Here, in order to conduct the simulations at minimum computational cost, a moisture content-based simulation approach is followed [38]. Also, as the cell moisture content reduces during drying, the turgor pressure is set to reduce in order to replicate actual plant cells during drying [37]. Furthermore, during drying, the moisture reduction from the cell wall and cell wall contraction effects are accounted [37].

2.4. Simulation of plant tissue drying (with case hardening)

In order to simulate tissue drying under the effect of case hardening, cells located at different cell layers are setup and simulated such that, compared to the outer boundary cells, the inner cell layers are moist. Accordingly, in each dried tissue state of the 23-cell tissue, only the outermost cell layer is

set to undergo 100% drying corresponding to a particular dryness state. Then the innermost cell is set to undergo only 75% of drying and the cells in the intermediate cell layer are set to undergo only 87.5% drying. Thereby, the tissue resembles a basic case hardening condition. To realise these differences in cell dryness, each cell in the corresponding cell layer is initiated with the respective moisture content, turgor pressure and cell wall mass values, and simulated according to the method mentioned in Section 2.3.

2.5. Computational implementation and model consistency

The above tissue model was programmed in a parallel C++ program and simulations were run on a High Performance Computer (HPC). The C++ source code was developed by referring to the algorithms of an existing FORTRAN-based SPH source code [22]. The model simulation results were visualised with the Open Visualization Tool (OVITO) [47]. During the simulations, model consistency error did not exceed 3% and density fluctuations were within 0.1% [38].

2.6. Experimental literature used for the model development and result interpretation

Most of the key physical properties used to model the above four plant food materials were directly adopted from literature and the others were set accordingly (see Table 1). For instance, the initial heights of the cylindrical cells were set by equating the volume of a cylindrical cell model to the volume of actual cells, assumed to be spherical. The pectin layer thickness was set proportional to the cell size. The pectin layer stiffness values were selected after a series of trial simulations leading to comparable initial cell shapes and cell-cell contacts in all of the four plant food materials used. In the case of grape and carrot, the cell wall shear modulus was set by assuming a comparable Young's modulus (E) of 100 MPa, at the corresponding cell wall thickness values (as given by Eq. A.2, the cell wall stiffness is mainly influenced by the product of the Young's modulus and the cell wall thickness). In the absence of corresponding literature data, turgor pressure of grape and potato cells were set equal to apple. Commonly for all of the plant materials, the magnitude of the osmotic potential was set equal to that of the corresponding fresh cell turgor pressure. In order to compare and validate the model predictions, several literature data were used as presented in Table 3. Depending on the availability of the experimental data, microscopic images of dried plant tissues were used to compare the model predictions qualitatively, and geometric parameters were used for quantitative comparisons (see Section 3 for details).

3. Results and discussion

3.1. Overall differences of plant tissue varieties as influenced by case hardening

As described in Section 2.4, four different plant tissue types were modelled and simulated for gradual drying (i.e. moisture content reduction), as presented in Fig. 5 and Fig. 6. From Fig. 5, it is clearly observed that tissues resemble the frequently observed honeycomb cellular structure of actual plant tissues. The darkness of the cell fluid colour indicates the level of normalised moisture that exists in different cell layers in the tissue. Therefore, since case hardening effect is omitted here, each tissue state indicates homogeneous moisture content across the tissue. When considering the tissue differences, potato tissue is considerably bigger due to the larger cell size compared to the apple and grape tissues. The carrot tissue is the smallest, since it has the smallest cell size. Fresh tissues commonly have higher turgor pressure and moisture content, which result in turgid cells. During drying, there are significant differences in the tissue shape and the deformation characteristics, which is mainly influenced by the differences of their physical properties as presented in Section 2.2. This is evident when the apple and grape tissue are considered, both have quite similar fresh cell sizes and initial configurations. During drying, however, the grape tissue undergoes a comparatively higher shrinkage than apple tissue, mainly due to the difference in the cell wall contraction effects (see Table 1). It is the same reason for the limited shrinkage of the potato tissue, where the cell wall contraction forces are not very significant. When referring to the carrot tissue, the inflated shape is mainly caused by the relatively higher turgor pressure present in the carrot tissues even at dried conditions. When this effect is combined with the intense cell wall contractions forces, the dried carrot tissue shrinkage pattern can be better understood.

When these tissues undergo shrinkage in the presence of case hardening as shown in Fig. 6, it is evident that high-moist cells exists towards the centre of the tissue, causing limited shrinkage when compared with the tissues with no case hardening (Fig. 5). This is a realistic phenomenon during drying, since the tissue directly interacts with the drying environment through the boundary cells, which are subjected to intensive moisture reduction in each drying state, compared to the inner cell layers. This forms a hardened case, which resists further moisture reduction from the interior cell layers of the tissue. Also, since higher turgor pressure values exist in the high-moist cells, the collapse of the cells is also limited, particularly in the interior cell layers. These eventually result in distinct changes of the cell wall wrinkling and other related geometrical parameters, which are discussed in detail in the below sections, with respect to each plant tissue type. Further, it should be noted here that, although diffusion-driven moisture content variation of the cells is not simulated here, these simulations provide an insight into the response of a plant tissue deformation during drying under case hardening.

3.2. Analysis of case hardening of apple tissue

Fig. 7 to Fig. 9 represent the distinct deformation characteristics of apple tissue undergoing drying with the direct influence of case hardening. Compared to Fig. 7, Fig. 8 indicates a limited shrinkage of the whole tissue which is evident by observing the tissue boundaries. In Fig. 8, the dried tissue states indicate the existence of different moisture content levels within the tissue, which eventually result in different cell shapes and cell wall wrinkling as presented in Fig. 9. It is clearly evident that interior cells of the case hardened tissue undergo minimum wrinkling when compared to the non-case hardened tissue, which is due to the higher moisture content and the turgor pressure existing in the interior cell layers. For instance, in these simulations, as described in Section 2.4, the centre cell is set to undergo only about 75% drying and the corresponding value for the intermediate cell layer is 87.5%. Accordingly, the turgor pressure is also higher in the interior cells, when compared to exterior cells or interior cells of non-case hardened tissues (Fig. 9(a)). In realistic drying experiments, these values can even be significant when bigger tissues with large numbers of cells are involved, causing considerable influence on cellular and tissue level deformation alterations. Further, these numerical results and cell deformations can be considered as comparable with the Scanning Electron Microscopy (SEM) images of apple tissues obtained from drying experiments as presented in Fig. 10 [14]. In the experiments, the tissue undergoes gradual shrinkage and increased cell wall wrinkling. However, from these images, it is quite difficult to identify a clear difference between cell sizes at different cell layers of the tissue. Therefore, in order to compare the numerical results with experiments, a quantitative study was conducted by referring to several cellular geometric parameters: cell area (A), Feret diameter[3] (D), perimeter (P), roundness[4] (R), elongation[5] (EL) and compactness[6] (C). Eventually, normalised parameters (X/X_0, A/A_0, D/D_0, P/P_0, R/R_0, EL/EL_0 and C/C_0) were used for the analysis, in order to facilitate easy comparison of the results as presented in Fig. 11. Particularly the reducing trends of the cell area, diameter and perimeter directly represent cellular shrinkage during drying. The reduction of the roundness and the compactness, and the increment of the elongation represents the in-homogeneous deformations of cells during drying [14]. The overall observation from these graphs is that there is an acceptable level of agreement between the experimental findings and the model predictions, implying that the modelling approach is sufficiently capable of modelling cellular shrinkage during drying. In the case of the influence of case hardening, only the cell area indicates some level of difference (although it not very significant), implying the limited shrinkage of tissues in the presence of case hardening. This insignificant quantitative difference is mainly due to the averaging of cell geometric parameters and normalised moisture contents, over the full tissue. Since, only the interior 7 cells out of 23 cells in the tissue contribute to

---

[3] $\sqrt{4A/\pi}$
[4] $4\pi A/P^2$
[5] $\sqrt{4A/\pi}$ /(major axis length)
[6] major axis length/minor axis length

any potential difference of the trends, the apparent quantitative difference can be expected to be quite minimal. However, in realistic tissue, since there are a large number of interior cells compared to boundary cells, the influence of the case hardening effect can be taken as distinguishable, in the quantitative terms. Although, these limitations exist in the quantitative measurements, there are still identifiable differences between tissue morphology in qualitative terms, as described previously in this section.

3.3. Analysis of case hardening of potato tissue

When referring to Fig. 12 and Fig. 13, the overall tissue shrinkage and level of cellular deformation can be considered as minimum, compared to the other tissue types. It is mainly due to the larger cell size and limited cell wall contraction forces (see Table 1). Further, when comparing Fig. 12 and Fig. 13, it is observed that only a very limited change is realised due to the case hardening, in the tissue morphology. However, the enlarged tissue configurations presented in Fig. 14 indicate that, the interior cells of the case hardened tissue are quite turgid, compared to the interior cells of the non-case hardened tissue. Even with the enlarged images, only a very limited tissue scale deformation difference is observed. Further, as presented in Fig. 15, the SEM images of the potato tissues during drying, only a limited cell wall wrinkling is observed compared to what is observed from the SEM images of apple tissues presented in Fig. 10. This trend is clearly replicated by the simulation results of the two tissue types in case of *without* case hardening and *with* case hardening. However, it is again difficult to clearly distinguish cellular morphological differences from these SEM images of potato tissues, which was the case even with the SEM images of apple tissues presented above.

When referring to the quantitative results as presented in Fig. 16, both the tissue simulations are quite identical, irrespective of the influence of case hardening. It basically implies that the meshfree-based modelling approach involved is sufficiently capable of modelling plant tissue during drying. However, there is hardly any identifiable quantitative difference of cellular geometric parameters caused by the case hardening effect, which was evident even with the qualitative tissue morphological observations described above for apple tissue. Particularly in the case of quantitative results, the limited number of cells used for the simulation can be considered as causing a significant influence, which was explained in Section 3.2 above. Further, when comparing Fig. 10 and Fig. 16, the level of shrinkage of potato cells is minimum to that of the apple cells during drying, which is also observed from simulation results and even with respective to the SEM images.

3.4. Analysis of case hardening of carrot tissue

As presented in Fig. 17, the carrot tissue undergoes significant deformation during drying with clearly identified local and tissue scale deformations, which are mainly driven by the higher turgor pressure existing in the cells and the intense cell wall contraction forces (see Table 1). When comparing Fig.

17 and Fig. 18, the influence of case hardening is clearly evident particularly when referring to the critically dried states (Fig. 17 (f) and Fig. 18 (f)). There, the outer cell layer resembles a hardened case and the inner cells are comparatively moist. Due to this moisture content variation, the interior cells are quite inflated and retain fairly high turgid nature, leading to minimum internal cellular deformations and cell wall wrinkling. This is further evident from the enlarged tissue simulation results presented in Fig. 19. This distinguishable difference is also observed from the quantitative results presented in Fig. 20. Although only a limited number of cells are used for this study, still the results confirm the limited shrinkage occurring in the carrot tissue during drying, due to the case hardening phenomena. Particularly with reference to the cell area and the Feret diameter, the difference of the shrinkage (i.e. cell size) is evident. However, the cell size difference is not clearly indicated by the cell perimeter, which is due to the error caused by averaging the perimeter values, as a large number of outer cells present in the tissue, compared to the interior cells, which process larger cell perimeters. Further, in the case of the case hardened carrot tissue, the average cell roundness and compactness have increased, and elongation has reduced, implying the comparative inflated nature of the cells and minimum cell wall wrinkling effects.

3.5. Analysis of case hardening of grape tissue

Fig. 21 and Fig. 22 correspond to grape tissue deformations during drying and compare the influence of case hardening. When referring to the colour coding, the influence of the case hardening phenomenon is clearly observed, both in local and tissue scale deformations, which can be explained in the same way as for the apple and potato tissue deformation characteristics. Particularly, Fig. 23 provides clear evidence of reduced cell wall wrinkling of the interior cells in the case hardened grape tissue. Also, it can be clearly observed that the shapes of the cells located at the outer tissue boundaries of the case hardened tissue are comparatively flattened when compared with the outer boundary cells of the non-case hardened tissue. Since the moisture contents of these outer cell layers of both of the tissue are almost identical, the shape difference should be a secondary effect of the shape change of the interior cells. Next, when the quantitative results are considered as presented in Fig. 24, the case hardened tissue shows comparatively lower shrinkage, particularly in the case of cell area, Feret diameter and roundness. Also, since a favourable agreement is observed from the model predictions and the experimental findings, the modelling approach can be considered as having sufficient capability to model cellular deformations of plant material during drying.

4. Conclusion and outlook

Using a 2-D meshfree-based plant tissue model, different plant tissue types were modelled with the objective of studying the influence of case hardening on cellular shrinkage during drying. The study focused on four plant tissue types: apple, potato, carrot and grape, and were simulated at different cell

moisture contents and turgor pressure values to achieve different dryness states. Due to various cellular characteristics, the various tissues responded to case hardening, differently. When compared with the experimental findings obtained from the literature, an acceptable agreement was observed both qualitatively and quantitatively, in most of the instances. The overall conclusions of the study are as follows:

- In the case hardened tissue, since high-moist cells exist in the inner regions of the tissues, those cells undergo limited shrinkage, producing limited cell wall wrinkling.
- The influence of case hardening on cellular shrinkage is more dominant in critically dried tissues.
- In all tissue types, moisture content mainly governs the level of case hardening and the relative difference of cellular deformations. Also, the physical location of the cells and the nature of intercellular bonds have a positive effect on the differences in cellular shrinkage under the influence of case hardening.
- For different tissue types, the influence of case hardening on shrinkage is mainly governed by the cell size, cell fluid turgor pressure, wall thickness, wall stiffness and wall contractions.
- Lager cell size or stiffer cell walls (higher cell wall Young's modulus or wall thickness) and higher turgor pressure, generally resist shrinkage, and therefore deformations of different cell layers are minimally influenced by case hardening. The trend is opposite in the case of higher cell wall contractions, where the difference in cellular shrinkage becomes clearly evident under the influence of case hardening.
- Even for the limited size of the tissue sample studied, the qualitative results clearly indicated the influence of case hardening on different cell layers. However, the quantitative results didn't indicate such a significant difference, which is due to the averaging of cellular parameters across the tissue, having a comparable number of internal and boundary cells. In the case of actual tissues, since larger numbers of internal cells exist when compared to case hardened boundary cells, the influence can expected to be significant, leading to quantifiable variations in geometric parameters.
- In most instances, model predictions indicated a strong agreement with the experimental findings. This implies the general applicability of the proposed modelling technique to model morphological changes in plant materials during drying.

With these findings, it is evident that the modelling technique used in this work has a good potential for further improvements, leading to an advanced numerical modelling technique useful for industrial drying applications to optimise both the product and the process. Realistic tissues can be modelled by aggregating larger numbers of cells in complex tissue structures, having heterogeneous cell shapes

and intercellular voids. Also, the meshfree formulation used for this tissue model has the potential to incorporate temperature-dependent case hardening and shrinkage characteristics.

5. Acknowledgements

6. References

1. Grabowski, S., M. Marcotte, and H.S. Ramaswamy, *Drying of Fruits, Vegetables, and Spices* in *Handbook of postharvest technology : cereals, fruits, vegetables, tea, and spices*, A. Chakraverty, et al., Editors. 2003, Marcel Dekker: New York p. 653-695.
2. Jangam, S.V., *An Overview of Recent Developments and Some R&D Challenges Related to Drying of Foods.* Drying Technology, 2011. **29**(12): p. 1343-1357.
3. Martin, O., et al., *Food Dehydration*, in *Handbook of Food Engineering, Second Edition*, R.H. Dennis and D.B. Lund, Editors. 2006, CRC Press. p. 601-744.
4. Lee, C.Y., D.K. Salunkhe, and F.S. Nury, *Some chemical and histological changes in dehydrated apple.* Journal of the Science of Food and Agriculture, 1967. **18**(3): p. 89-93.
5. Hills, B.P. and B. Remigereau, *NMR studies of changes in subcellular water compartmentation in parenchyma apple tissue during drying and freezing.* International Journal of Food Science & Technology, 1997. **32**(1): p. 51-61.
6. Lewicki, P.P. and J. Drzewucka-Bujak. *Effect of drying on tissue structure of selected fruits and vegetables.* in *Proceedings of the 11th International Drying Symposium Drying (IDS'98).* 1998. Greece: Ziti Editions Thessaloniki.
7. Ramos, I.N., et al., *Quantification of microstructural changes during first stage air drying of grape tissue.* Journal of Food Engineering, 2004. **62**(2): p. 159-164.
8. Mayor, L., M.A. Silva, and A.M. Sereno, *Microstructural Changes during Drying of Apple Slices.* Drying Technology, 2005. **23**(9-11): p. 2261-2276.
9. Witrowa-Rajchert, D. and M. Rząca, *Effect of Drying Method on the Microstructure and Physical Properties of Dried Apples.* Drying Technology, 2009. **27**(7-8): p. 903-909.
10. Han, Q.-H., et al., *Optimization of Process Parameters for Microwave Vacuum Drying of Apple Slices Using Response Surface Method.* Drying Technology, 2010. **28**(4): p. 523-532.
11. Sabarez, H.T., J.A. Gallego-Juarez, and E. Riera, *Ultrasonic-Assisted Convective Drying of Apple Slices.* Drying Technology, 2012. **30**(9): p. 989-997.
12. Lozano, J.E., E. Rotstein, and M.J. Urbicain, *Total porosity and open-pore porosity in the drying of fruits.* Journal of Food Science, 1980. **45**(5): p. 1403-1407.
13. Lewicki, P.P. and G. Pawlak, *Effect of Drying on Microstructure of Plant Tissue.* Drying Technology, 2003. **21**(4): p. 657-683.

14. Karunasena, H.C.P., et al., *Scanning Electron Microscopic Study of Microstructure of Gala Apples During Hot Air Drying.* Drying Technology, 2014a. **32**(4): p. 455-468.

15. Bai, Y., et al., *Structural Changes in Apple Rings during Convection Air-Drying with Controlled Temperature and Humidity.* Journal of Agricultural and Food Chemistry, 2002. **50**(11): p. 3179-3185.

16. Rahman, M.S., I. Al-Zakwani, and N. Guizani, *Pore formation in apple during air-drying as a function of temperature: porosity and pore-size distribution.* Journal of the Science of Food and Agriculture, 2005. **85**(6): p. 979-989.

17. Funebo, T., et al., *Microwave heat treatment of apple before air dehydration – effects on physical properties and microstructure.* Journal of Food Engineering, 2000. **46**(3): p. 173-182.

18. Bartlett, M.K., C. Scoffoni, and L. Sack, *The determinants of leaf turgor loss point and prediction of drought tolerance of species and biomes: a global meta-analysis.* Ecology Letters, 2012. **15**(5): p. 393-405.

19. Mayor, L. and A.M. Sereno, *Modelling shrinkage during convective drying of food materials: a review.* Journal of Food Engineering, 2004. **61**(3): p. 373-386.

20. Zhu, H.X. and J.R. Melrose, *A Mechanics Model for the Compression of Plant and Vegetative Tissues.* Journal of Theoretical Biology, 2003. **221**(1): p. 89-101.

21. Crapiste, G.H., S. Whitaker, and E. Rotstein, *Drying of cellular material—I. A mass transfer theory.* Chemical Engineering Science, 1988-a. **43**(11): p. 2919-2928.

22. Liu, G.R. and M.B. Liu, *Smoothed Particle Hydrodynamics : A Meshfree Particle Method*. 2003, Singapore: World Scientific Publishing Co. 445.

23. Liu, Z., et al., *Modeling and simulation of buckling of polymeric membrane thin film gel.* Computational Materials Science, 2010. **49**(1, Supplement): p. S60-S64.

24. Jeong, S., S.-H. Park, and C.-H. Kim, *Simulation of Morphology Changes in Drying Leaves.* Computer Graphics Forum, 2013. **32**(1): p. 204-215.

25. Karunasena, H.C.P., et al., *A Particle Based Model to Simulate Microscale Morphological Changes of Plant Tissues during Drying.* Soft Matter, 2014e. **10**(29): p. 5249-5268.

26. Wang, C.X., L. Wang, and C.R. Thomas, *Modelling the Mechanical Properties of Single Suspension-Cultured Tomato Cells.* Annals of Botany, 2004. **93**(4): p. 443-453.

27. Wu, N. and M.J. Pitts, *Development and validation of a finite element model of an apple fruit cell.* Postharvest Biology and Technology, 1999. **16**(1): p. 1-8.

28. Gao, Q. and R.E. Pitt, *Mechanics of parenchyma tissue based on cell orientation and microstructure.* Transactions of the ASABE, 1991. **34**(1): p. 0232-0238.

29. Pitt, R.E., *Models for the Rheology and Statistical Strength of Uniformly Stressed Vegetative Tissue.* Transactions of the ASABE, 1982. **25**(6): p. 1776-1784.

30. Honda, H., M. Tanemura, and T. Nagai, *A three-dimensional vertex dynamics cell model of space-filling polyhedra simulating cell behavior in a cell aggregate.* Journal of Theoretical Biology, 2004. **226**(4): p. 439-453.

31. Rudge, T. and J. Haseloff, *A Computational Model of Cellular Morphogenesis in Plants*, in *Advances in Artificial Life*, M. Capcarrère, et al., Editors. 2005, Springer Berlin Heidelberg. p. 78-87.

32. Fanta, S.W., et al., *Microscale modeling of coupled water transport and mechanical deformation of fruit tissue during dehydration.* Journal of Food Engineering, 2014. **124**(0): p. 86-96.

33. Frank, X. and P. Perré, *The Potential of Meshless Methods to Address Physical and Mechanical Phenomena Involved during Drying at the Pore Level.* Drying Technology, 2010. **28**(8): p. 932-943.

34. Van Liedekerke, P., et al., *Mechanisms of soft cellular tissue bruising. A particle based simulation approach.* Soft Matter, 2011. **7**(7): p. 3580-3591.

35. Liedekerke, P.V., et al., *A particle-based model to simulate the micromechanics of single-plant parenchyma cells and aggregates.* Physical Biology, 2010. **7**(2): p. 026006.

36. Van Liedekerke, P., et al., *Particle-based model to simulate the micromechanics of biological cells.* Physical Review E, 2010. **81**(6): p. 061906.

37. Karunasena, H.C.P., et al., *Simulation of plant cell shrinkage during drying – A SPH–DEM approach.* Engineering Analysis with Boundary Elements, 2014c. **44**(0): p. 1-18.

38. Karunasena, H.C.P., et al., *A Coupled SPH-DEM Model for Micro-scale Structural Deformations of Plant Cells during Drying.* Applied Mathematical Modelling, 2014b. **38**(15-16): p. 3781-3801.

39. Karunasena, H.C.P., et al. *A Coupled SPH-DEM Model for Fluid and Solid Mechanics of Apple Parenchyma Cells During Drying.* in *18th Australian Fluid Mechanics Conference.* 2012d. Launceston - Australia: Australasian Fluid Mechanics Society.

40. Karunasena, H.C.P., et al. *A particle based micromechanics model to simulate drying behaviors of vegetable cells.* in *4th International Conference on Computational Methods (ICCM 2012).* 2012c. Gold Coast, Australia.

41. Karunasena, H.C.P., et al., *A Meshfree Model for Plant Tissue Deformations during Drying.* ANZIAM Journal, 2014d. **55 (EMAC2013)**: p. C110-C137.

42. Gingold, R.A. and J.J. Monaghan, *Smoothed particle hydrodynamics - Theory and application to non-spherical stars.* Monthly Notices of the Royal Astronomical Society, 1977. **181**: p. 375-389.

43. Wang, N. and J.G. Brennan, *Changes in structure, density and porosity of potato during dehydration.* Journal of Food Engineering, 1995. **24**(1): p. 61-76.

44. Karathanos, V.T., G. Villalobos, and G.D. Saravacos, *Comparison of Two Methods of Estimation of the Effective Moisture Diffusivity from Drying Data.* Journal of Food Science, 1990. **55**(1): p. 218-223.

45. Karunasena, H.C.P., et al., *A Novel Approach for Numerical Simulation of Plant Tissue Shrinkage During Drying*, in *International Research Symposium on Postharvest Technology*, B.M.K.S. Thilakarathne, et al., Editors. 2014f, Research and Development Centre, Institute of Post Harvest Technology: Anuradapura, Sri Lanka. p. 130-135.

46. Colagrossi, A., et al., *Particle packing algorithm for SPH schemes.* Computer Physics Communications, 2012. **183**(8): p. 1641-1653.

47. Stukowski, A., *Visualization and analysis of atomistic simulation data with OVITO–the Open Visualization Tool.* Modelling and Simulation in Materials Science and Engineering, 2010. **18**(1): p. 015012.

48. Hepworth, D.G. and D.M. Bruce, *Measuring the Deformation of Cells within a Piece of Compressed Potato Tuber Tissue.* Annals of Botany, 2000. **86**(2): p. 287-292.

49. Lewicki, P.P. and G. Pawlak, *Effect of Mode of Drying on Microstructure of Potato.* Drying Technology, 2005. **23**(4): p. 847-869.

50. McGarry, A., *Cellular Basis of Tissue Toughness in Carrot (Daucus carota L.) Storage Roots.* Annals of Botany, 1995. **75**(2): p. 157-163.

51. Sansiribhan, S., S. Devahastin, and S. Soponronnarit, *Quantitative Evaluation of Microstructural Changes and their Relations with Some Physical Characteristics of Food during Drying.* Journal of Food Science, 2010. **75**(7): p. E453-E461.

52. Schlosser, J., et al., *Cellular expansion and gene expression in the developing grape (Vitis vinifera L.).* Protoplasma, 2008. **232**(3-4): p. 255-265.

53. Georget, D.M.R., A.C. Smith, and K.W. Waldron, *Modelling of carrot tissue as a fluid-filled foam.* Journal of Materials Science, 2003. **38**(9): p. 1933-1938.

54. Hiller, S., D.M. Bruce, and G. Jeronimidis, *A micro-penetration technique for mechanical testing of plant cell walls.* Journal of Texture Studies, 1996. **27**(5): p. 559-587.

55. Campos-Mendiola, R., et al., *Non-isotropic shrinkage and interfaces during convective drying of potato slabs within the frame of the systematic approach to food engineering systems (SAFES) methodology.* Journal of Food Engineering, 2007. **83**(2): p. 285-292.

56. Ramos, M.I.F.N., *Integrated Approach on Field Solar Drying, Pilot Convective Drying and Microstructural Changes*, in *School of Biotechnology.* 2010, Catholic University of Portugal Porto - Portugal.

57. McGarry, A., *Influence of Water Status on Carrot (Daucus Carota L.) Fracture Properties.* Journal of Horticultural Science & Biotechnology, 1993. **68**(3): p. 431-438.

58. Sansiribhan, S., S. Devahastin, and S. Soponronnarit, *Generalized microstructural change and structure-quality indicators of a food product undergoing different drying methods and conditions.* Journal of Food Engineering, 2012. **109**(1): p. 148-154.

59. Taiz, L. and E. Zeiger, *Water and Plant Cells*, in *Plant Physiology*. 2010, Sinauer Associates, Sunderland, USA. p. 73-84.
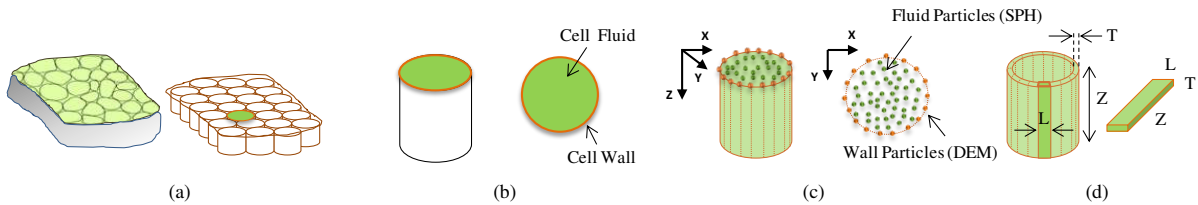
7. Figures and tables

Fig. 1. (a) A plant tissue simply represented as an aggregate of cylindrical cells, (b) 2-D model to represent any cylindrical cell; (c) particle scheme used for the 2-D Cell model: fluid model based on SPH particles and wall model based on DEM particles; and (d) discrete elements of the cell wall.
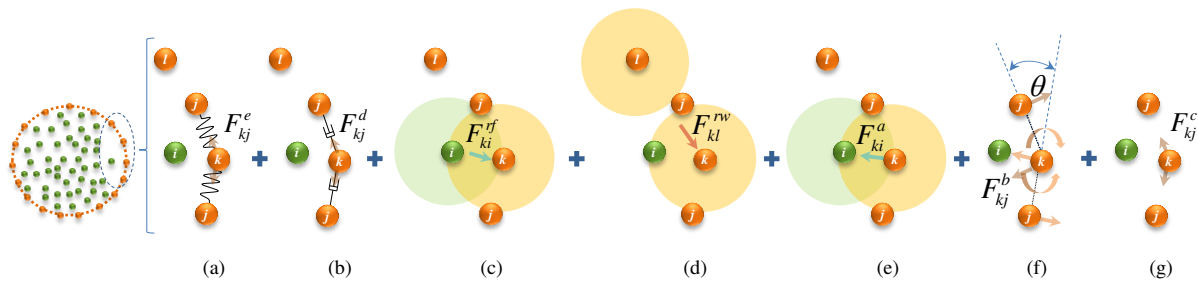

Fig. 2. Force interactions used in the DEM-based cell wall model: wall stiff forces (F_{kj}^e), wall damping forces (F_{kj}^d), wall-fluid repulsion forces (F_{ki}^{rf}), non-bonded wall-wall repulsion forces (F_{kl}^{rw}), wall-fluid attraction forces (F_{ki}^a), forces due to wall bending stiffness (F_{kj}^b), and forces for cell wall contractions during drying (F_{kj}^c). (i : fluid particles; j, k & l : wall particles)

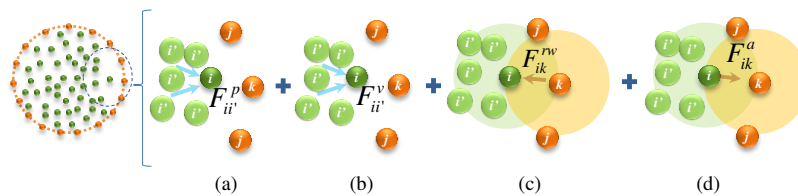

Fig. 3. Force interactions used in the SPH-based cell fluid model: pressure force ($F_{ii'}^p$), viscous force ($F_{ii'}^v$), wall-fluid repulsion forces (F_{ik}^{rw}), and wall-fluid attraction forces (F_{ik}^a). (i & i' : fluid particles; j & k: wall particles)

Fig. 4. Tissue model and cell-cell force interactions: (a) hexagonal shaped cells are used for tissue initialisation with positive pectin layer gap; (b) interacting wall particle pairs of adjacent cells; (c) pectin layer stiff forces ($F_{km}^{e\_pectin}$); and (d) cell-cell repulsion forces (F_{km}^{rc}). (i: fluid particles; k & m: wall particles)

Table 1 Customised model parameters for different plant materials

| Parameter | Food variety used for modelling | | | |
| | Apple | Potato | Carrot | Grape |
	Value (Source)	Value (Source)	Value (Source)	Value (Source)
Initial cell diameter (D_0)	150 μm [14]	200 μm [48, 49]	100 μm [6, 50, 51]	150 μm [52]
Initial cell height (Z_0)	100 μm (= 2/3 D_0)	133 μm (= 2/3 D_0)	53 μm (= 2/3 D_0)	100 μm (= 2/3 D_0)
Wall initial thickness (T_0)	6 μm [27, 35]	1 μm [48]	2 μm [50, 53]	3 μm [52]
Pectin layer thickness (T_p)	8 μm (set)	10 μm (set)	4 μm (set)	8 μm (set)
Pectin layer stiffness (k_{pectin})	20 N m^{-1} (set)	20 N m^{-1} (set)	10 N m^{-1} (set)	20 N m^{-1} (set)
Wall shear modulus (G) ≈ $E/3$	18 MPa [27, 35]	166 MPa [48, 54]	33 MPa (set)	33 MPa (set)
Empirical factors on cell wall contraction (a, b)	0.2, 0.9 [14]	0.07, 0.92 [55]	0.36, 0.93 [51]	0.18, 0.43 [56]
Fresh cell turgor pressure (P$_T$)	200 kPa [35]	200 kPa (set)	400 kPa [57]	200 kPa (set)
Fresh cell osmotic potential (Π)	-200 kPa (= $-P_T$)	-200 kPa (= $-P_T$)	-400 kPa (= $-P_T$)	-200 kPa (= $-P_T$)

Table 2 Commonly used model parameters for all plant materials

Parameter	Value	Source
Fluid viscosity (μ)	0.1 Pa s	set [35]
Initial fluid density (ρ_0)	1000 kg m^{-3}	set [35]
Wall permeability (L_P)	2.5 × 10^{-6} m^2 N^{-1} s	set [38]
Wall bending stiffness (k_b)	1 × 10^{-12} N m rad^{-1}	set [25]
Wall damping ratio (γ)	5 × 10^{-6} N m^{-1} s	set [38]
Fluid compression modulus (K)	20 MPa	set [38]
Wall contraction force coefficient (k_{wc})	4 × 10^4 N m^{-1}	set [25]
LJ contact strength for wall-fluid repulsions (f_0^{rf})	1 × 10^{-12} N m^{-1}	set [25]
LJ contact strength for wall-wall repulsions (f_0^{rw})	1 × 10^{-12} N m^{-1}	set [25]
LJ contact strength for wall-fluid attractions (f_0^{a})	2 × 10^{-12} N m^{-1}	set [25]
LJ contact strength for cell-cell repulsions (f_0^{rc})	1 × 10^{-10} N m^{-1}	set [25]
Initial smoothing length (h_0)	1.2 × initial fluid grid spacing	set [25]
Time step (Δt)	2 × 10^{-9} s	set [25]

Table 3 Literature data used for qualitative and quantitative model validation

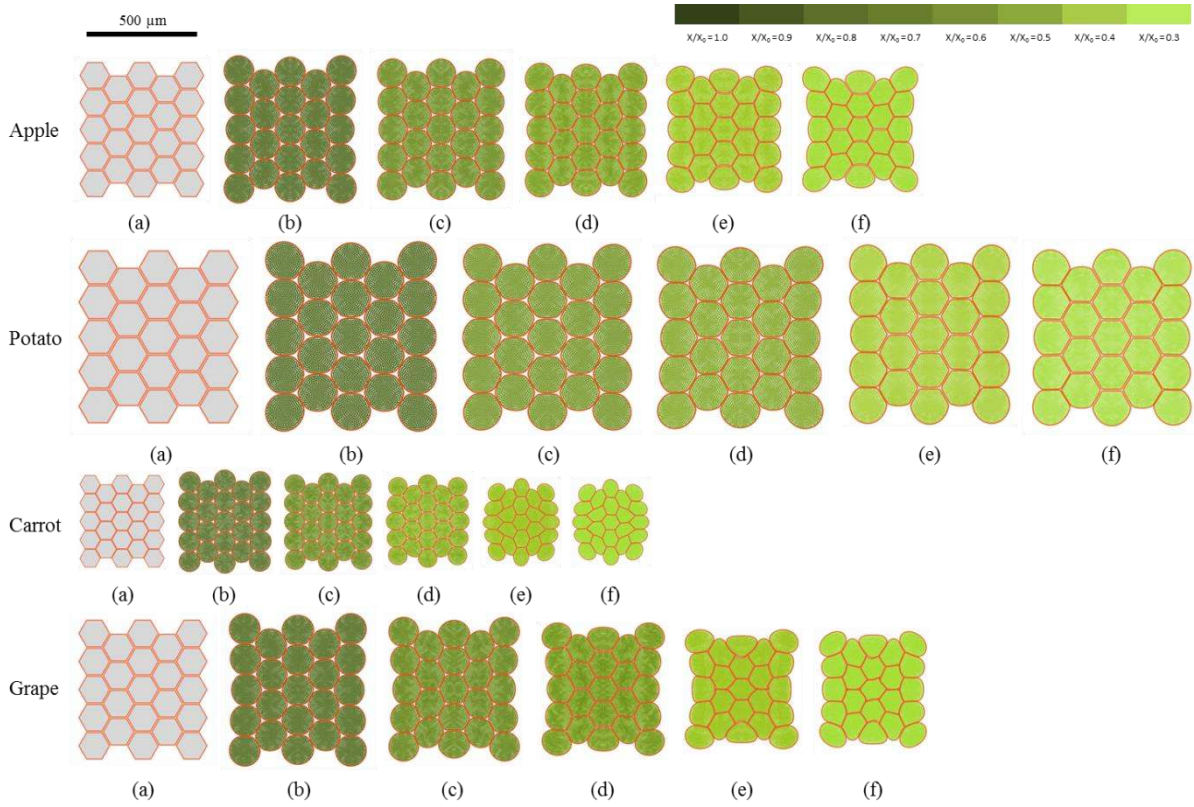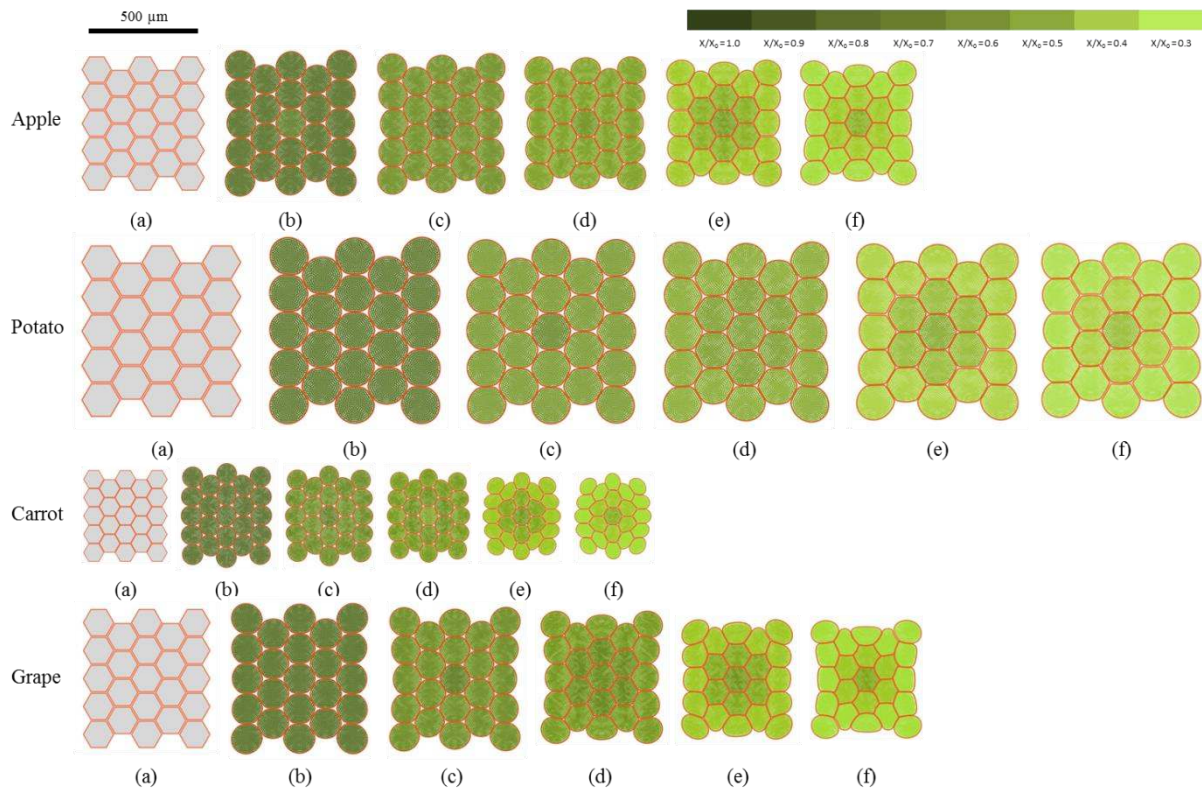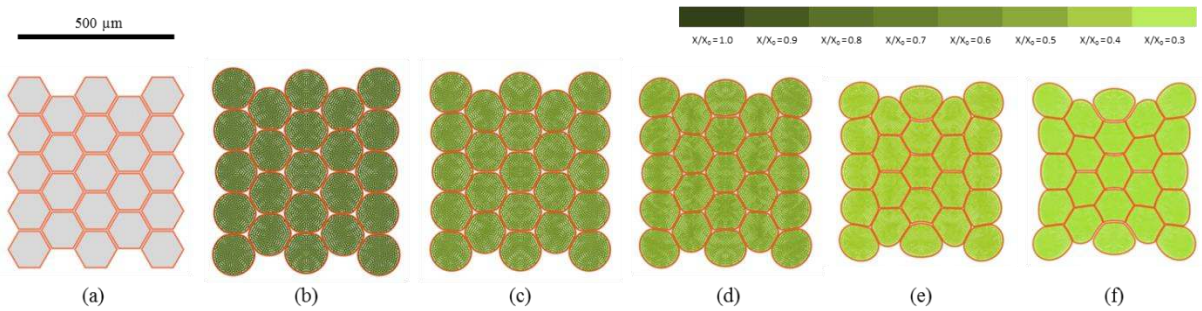| Plant variety | Qualitative data (microscopy images) | Quantitative data | | | | | |
		A	D	P	R	EL	C
Apple	[14]	[14]	[14]	[14]	[14]	[14]	[14]
Potato	Our experiments	[55]	[55]	[55]	[49]	-	-
Carrot	[58]	[51]	[51]	[51]	-	-	-
Grapes	[7]	[7, 56]	[7, 56]	[7, 56]	[7, 56]	[7, 56]	[7, 56]

Fig. 5. Tissue simulations at different states of dryness (without case hardening): (a) initial condition before simulations, (b) X/X_0 = 1.0, (c) X/X_0 = 0.8, (d) X/X_0 = 0.6, (e) X/X_0 = 0.4, and (f) X/X_0 = 0.3. (these X/X_0 values correspond to any cell in the tissue)
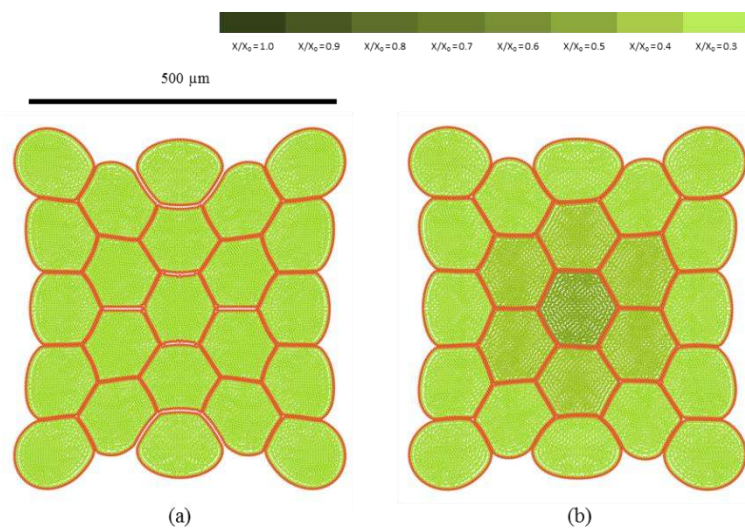
Fig. 6. Tissue simulations at different states of dryness (with case hardening): (a) initial condition before simulations, (b) $X/X_0 = 1.0$, (c) $X/X_0 = 0.8$, (d) $X/X_0 = 0.6$, (e) $X/X_0 = 0.4$, and (f) $X/X_0 = 0.3$. (these X/X_0 values correspond to any cell at the tissue boundary)
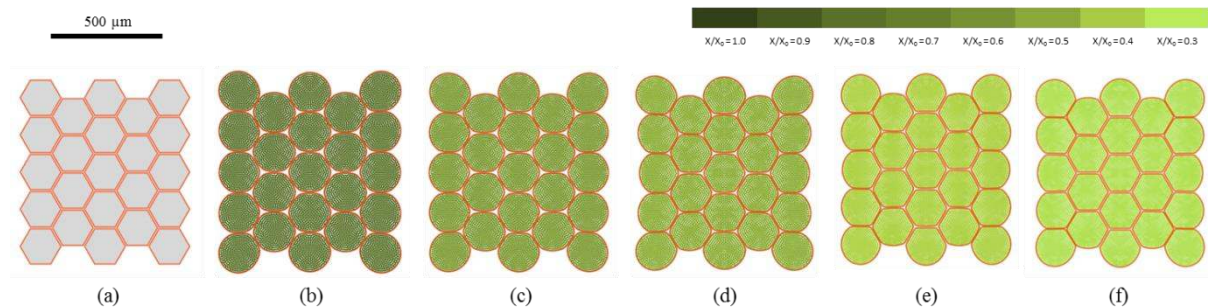

Fig. 7. Apple tissue simulations at different states of dryness (without case hardening): (a) initial condition before simulations, (b) $X/X_0 = 1.0$, (c) $X/X_0 = 0.8$, (d) $X/X_0 = 0.6$, (e) $X/X_0 = 0.4$, and (f) $X/X_0 = 0.3$. (these X/X_0 values correspond to any cell in the tissue)
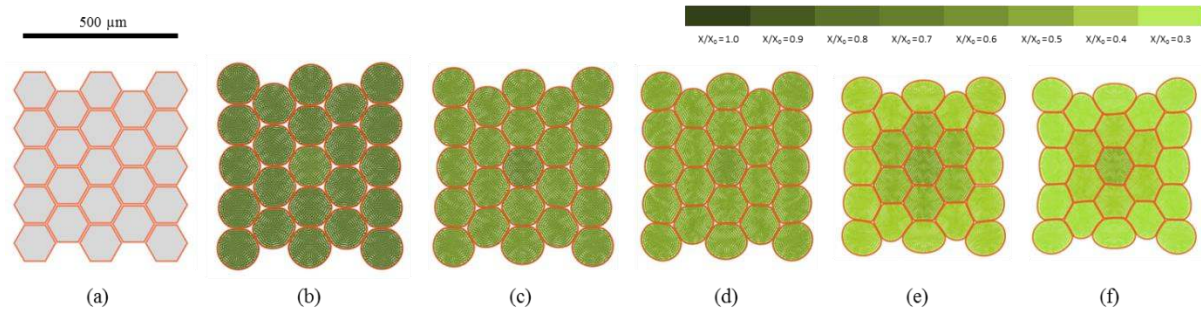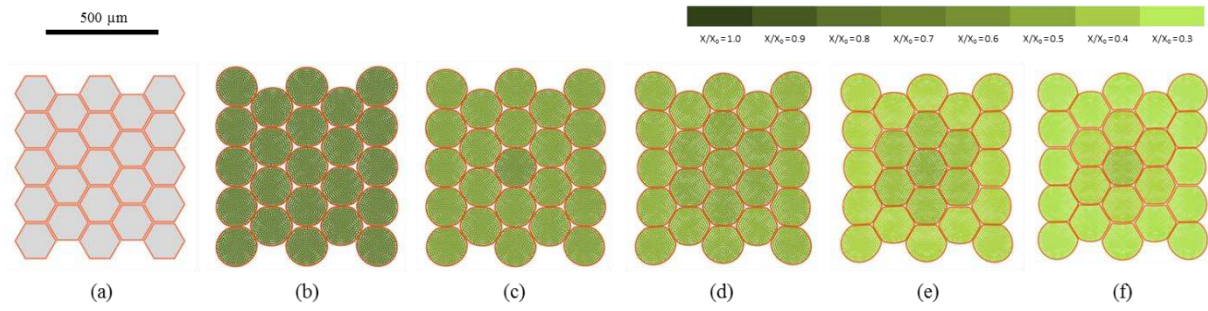
Fig. 8. Apple tissue simulations at different states of dryness (with case hardening): (a) initial condition before simulations, (b) X/X_0= 1.0, (c) X/X_0 = 0.8, (d) X/X_0 = 0.6, (e) X/X_0 = 0.4, and (f) X/X_0 = 0.3. (these X/X_0 values correspond to any cell at the tissue boundary)
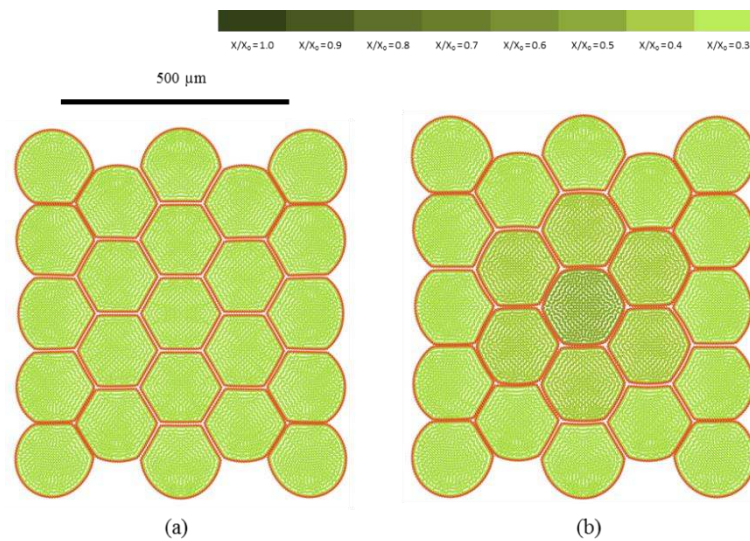

Fig. 9. Apple tissue simulations (enlarged view): (a) without case hardening at X/X_0 = 0.3, and (b) with case hardening at X/X_0 = 0.3 (corresponds to any cell at the tissue boundary).
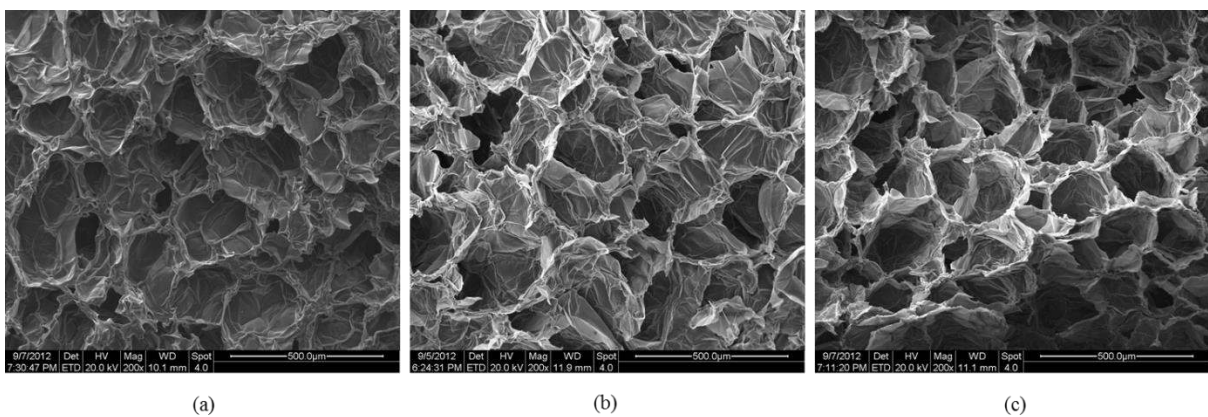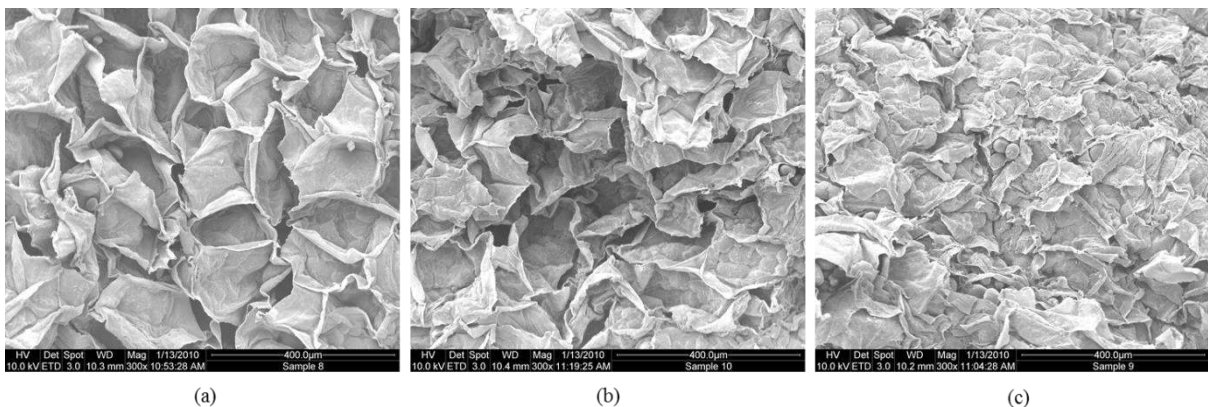

Fig. 10. Scanning Electron Microscopy (SEM) images of apple tissues at different states of dryness (with case hardening): (a) X/X_0= 1.0, (b) X/X_0 = 0.5, and (c) X/X_0 = 0.2. (bar is 500 µm) [14]
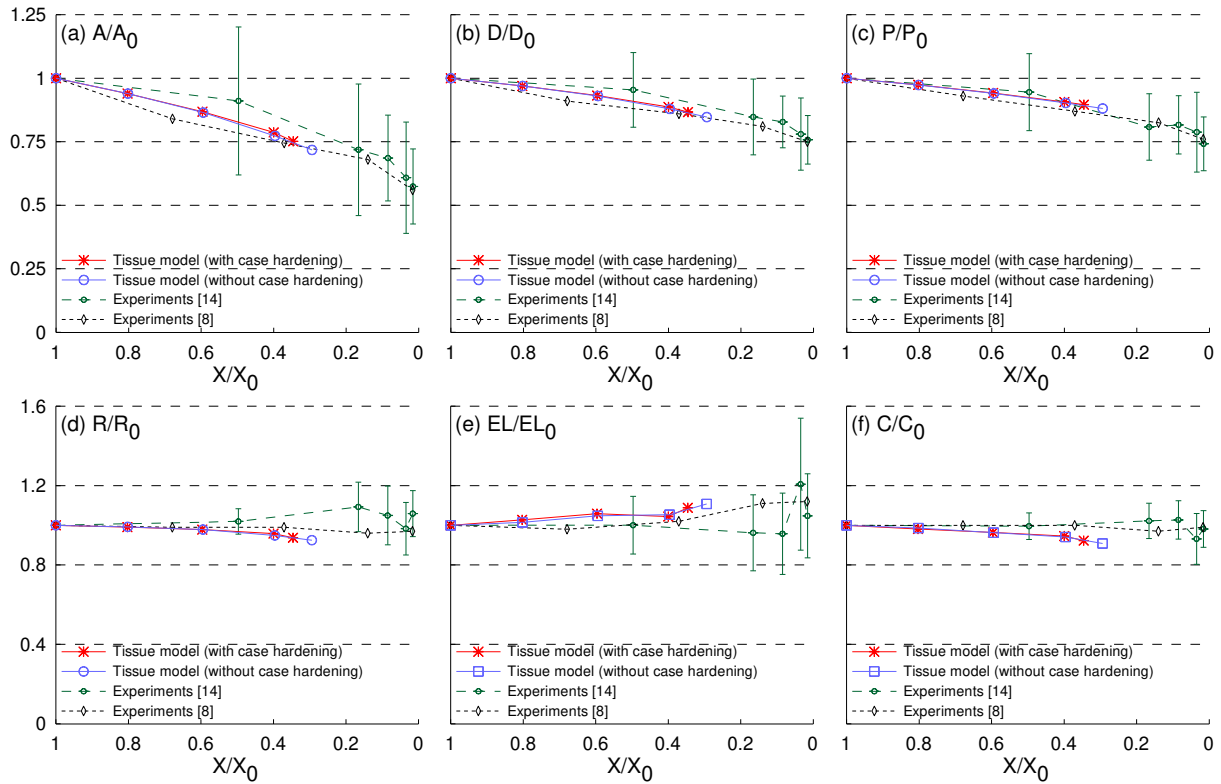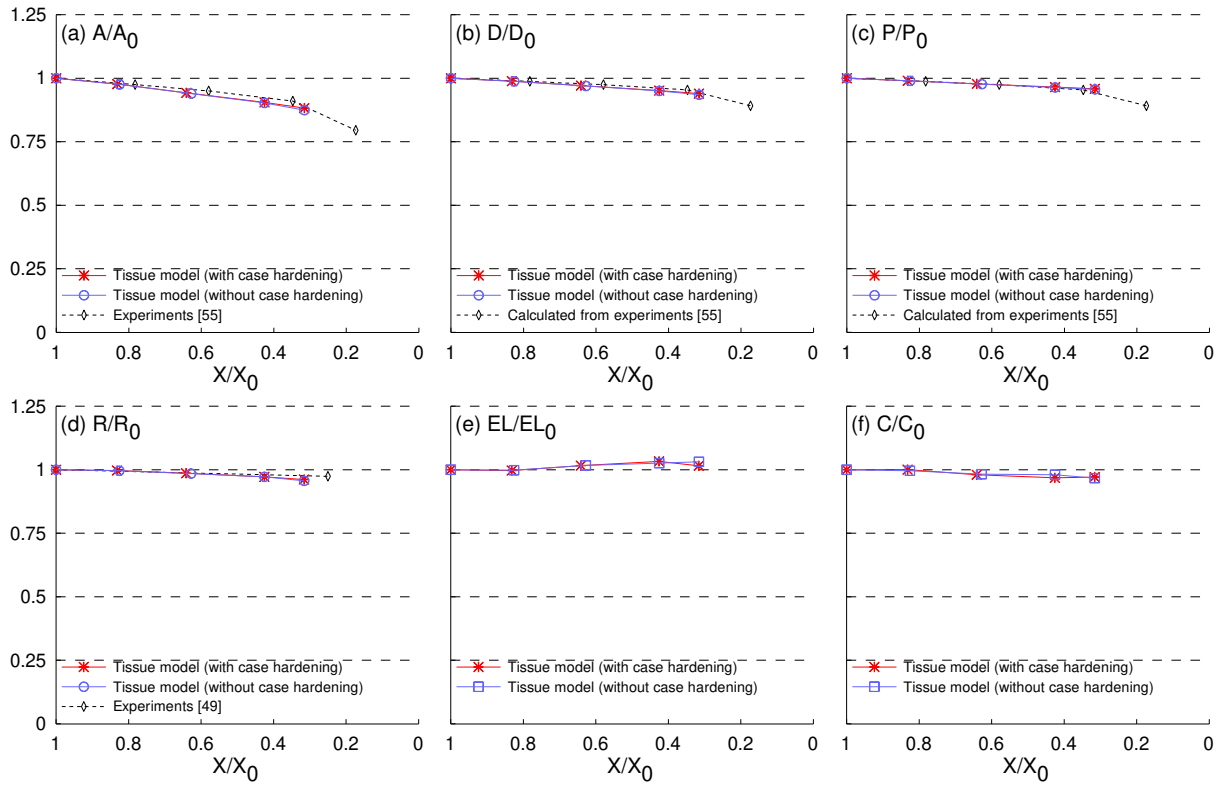
Fig. 11. Influence of case hardening for cellular geometrical parameter variations of apple tissues during drying: (a) A/A_0, (b) D/D_0, (c) P/P_0, (d) R/R_0, (e) EL/EL_0, and (f) C/C_0. (X/X_0 represents the overall average of the normalised moisture content, considering all the cells in the tissue)

Fig. 12. Potato tissue simulations at different states of dryness (without case hardening): (a) initial condition before simulations, (b) $X/X_0 = 1.0$, (c) $X/X_0 = 0.8$, (d) $X/X_0 = 0.6$, (e) $X/X_0 = 0.4$, and (f) $X/X_0 = 0.3$. (these X/X_0 values correspond to any cell in the tissue)

Fig. 13. Potato tissue simulations at different states of dryness (with case hardening): (a) initial condition before simulations, (b) X/X_0= 1.0, (c) X/X_0 = 0.8, (d) X/X_0 = 0.6, (e) X/X_0 = 0.4, and (f) X/X_0 = 0.3. (these X/X_0 values correspond to any cell at the tissue boundary)

Fig. 14. Potato tissue simulations (enlarged view): (a) without case hardening at $X/X_0 = 0.3$, and (b) with case hardening at $X/X_0 = 0.3$ (corresponds to any cell at the tissue boundary).

Fig. 15. SEM images of potato tissues at different states of dryness (with case hardening): (a) X/X_0= 1.0, (b) X/X_0 = 0.5, and (c) X/X_0 = 0.3. (bar is 400 μm)

Fig. 16. Influence of case hardening for cellular geometrical parameter variations of potato tissues during drying: (a) A/A_0, (b) D/D_0, (c) P/P_0, (d) R/R_0, (e) EL/EL_0, and (f) C/C_0. (X/X_0 represents the overall average of the normalised moisture content, considering all the cells in the tissue)
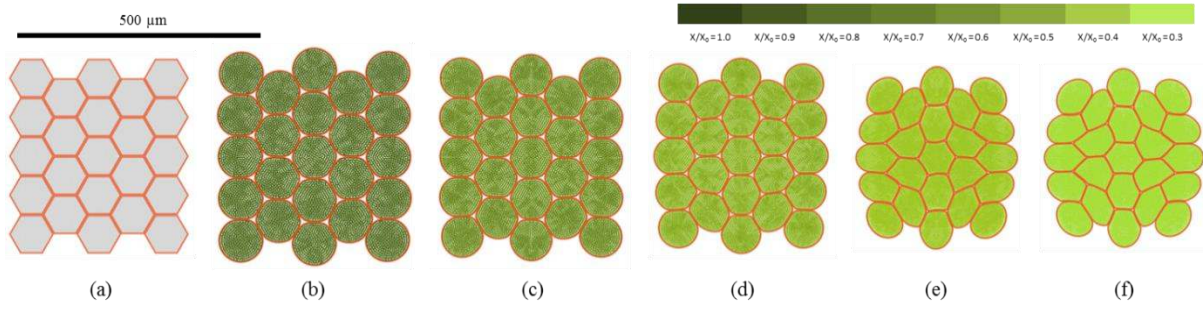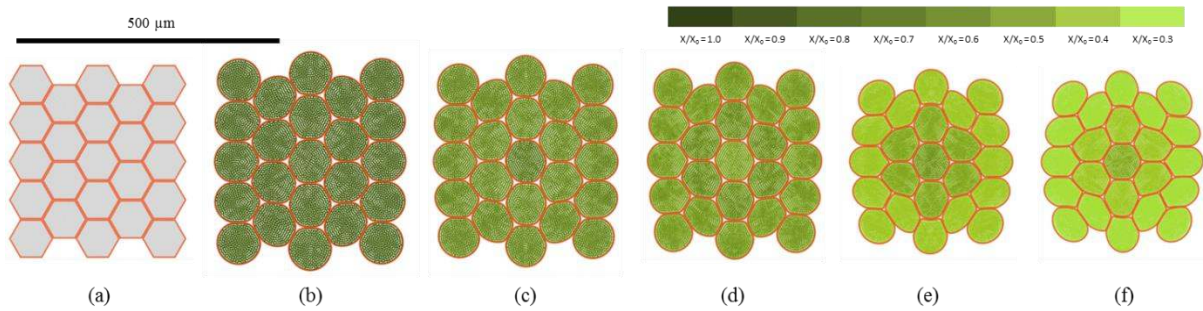
Fig. 17. Carrot tissue simulations at different states of dryness (without case hardening): (a) initial condition before simulations, (b) X/X_0= 1.0, (c) X/X_0 = 0.8, (d) X/X_0 = 0.6, (e) X/X_0 = 0.4, and (f) X/X_0 = 0.3. (these X/X_0 values correspond to any cell in the tissue)

Fig. 18. Carrot tissue simulations at different states of dryness (with case hardening): (a) initial condition before simulations, (b) X/X_0= 1.0, (c) X/X_0 = 0.8, (d) X/X_0 = 0.6, (e) X/X_0 = 0.4, and (f) X/X_0 = 0.3. (these X/X_0 values correspond to any cell at the tissue boundary)
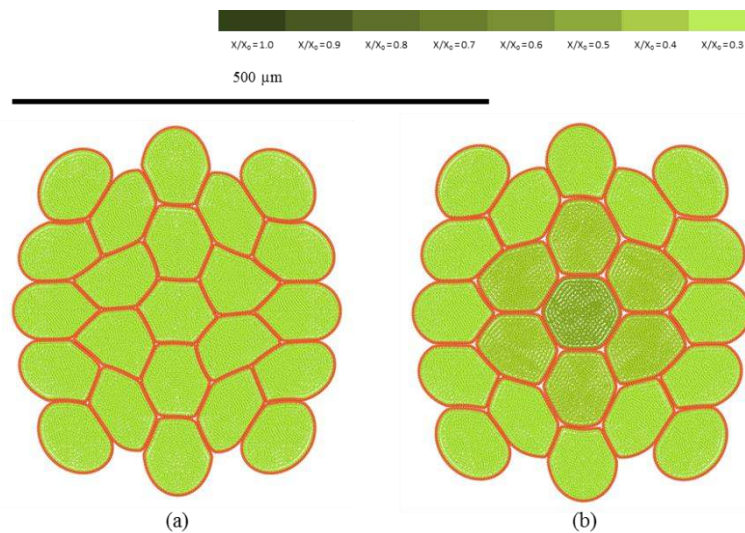

Fig. 19. Carrot tissue simulations (enlarged view): (a) without case hardening at $X/X_0 = 0.3$, and (b) with case hardening at $X/X_0 = 0.3$ (corresponds to any cell at the tissue boundary).
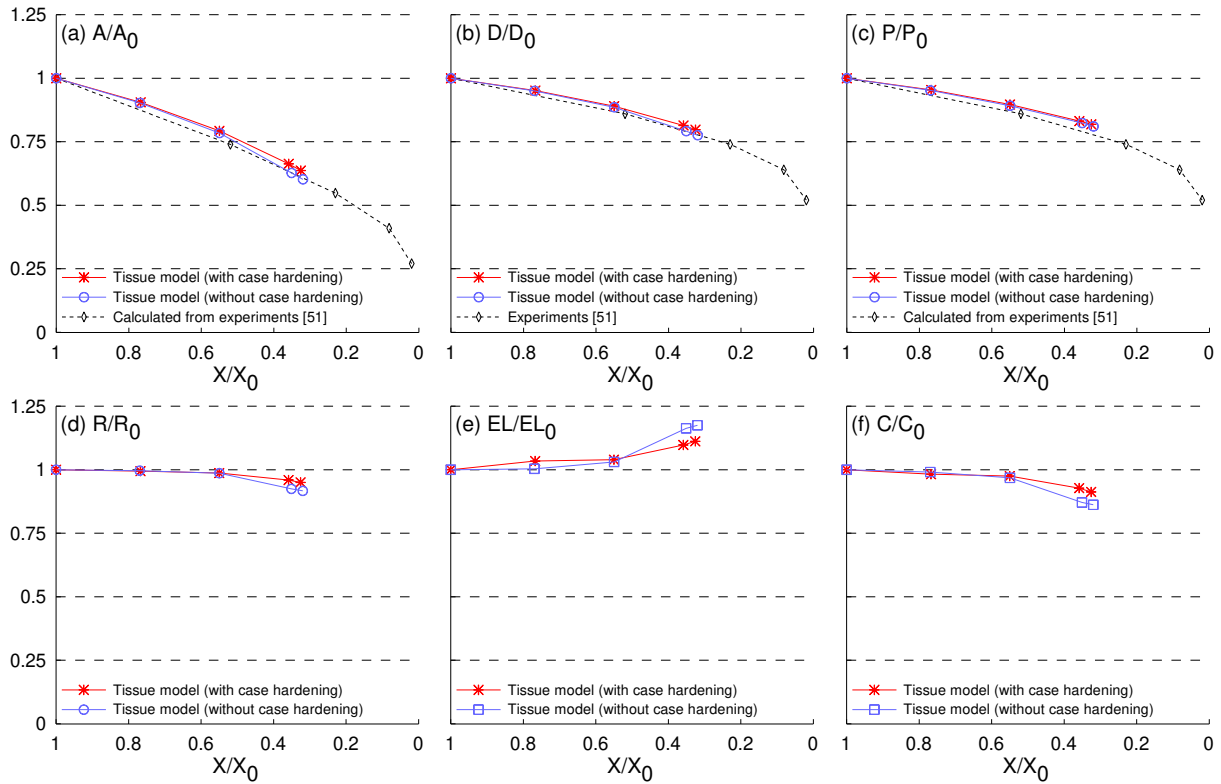
Fig. 20. Influence of case hardening for cellular geometrical parameter variations of carrot tissues during drying: (a) A/A_0, (b) D/D_0, (c) P/P_0, (d) R/R_0, (e) EL/EL_0, and (f) C/C_0. (X/X_0 represents the overall average of the normalised moisture content, considering all the cells in the tissue)

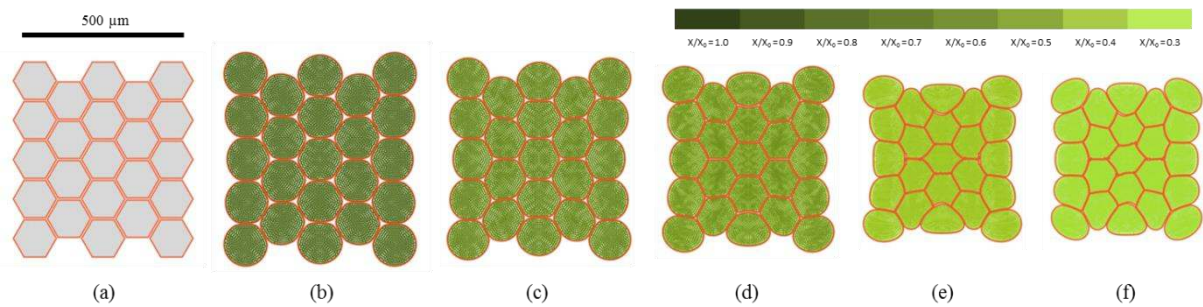Fig. 21. Grape tissue simulations at different states of dryness (without case hardening): (a) initial condition before simulations, (b) X/X_0= 1.0, (c) X/X_0 = 0.8, (d) X/X_0 = 0.6, (e) X/X_0 = 0.4, and (f) X/X_0 = 0.3. (these X/X_0 values correspond to any cell in the tissue)
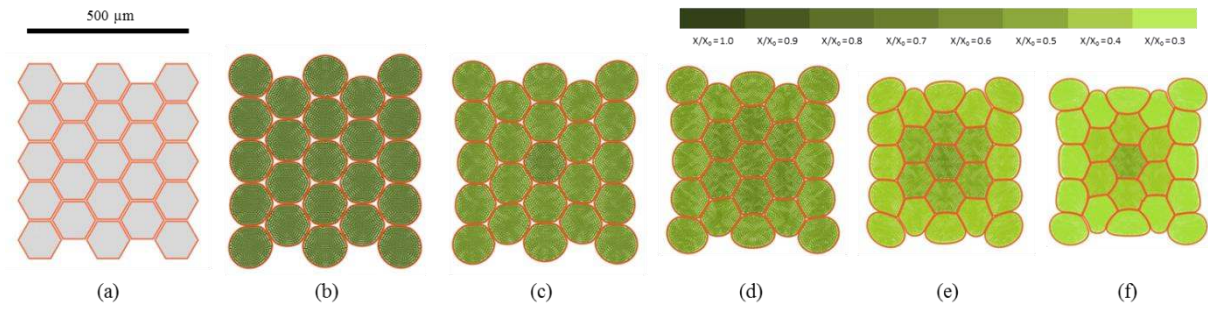
Fig. 22. Grape tissue simulations at different states of dryness (with case hardening): (a) initial condition before simulations, (b) X/X_0 = 1.0, (c) X/X_0 = 0.8, (d) X/X_0 = 0.6, (e) X/X_0 = 0.4, and (f) X/X_0 = 0.3. (these X/X_0 values correspond to any cell at the tissue boundary)
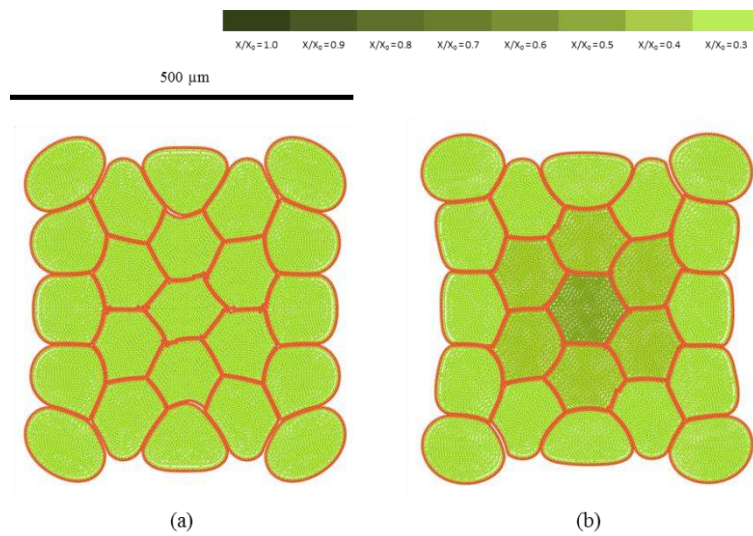

Fig. 23. Grape tissue simulations (enlarged view): (a) without case hardening at X/X_0 = 0.3, and (b) with case hardening at X/X_0 = 0.3 (corresponds to any cell at the tissue boundary).
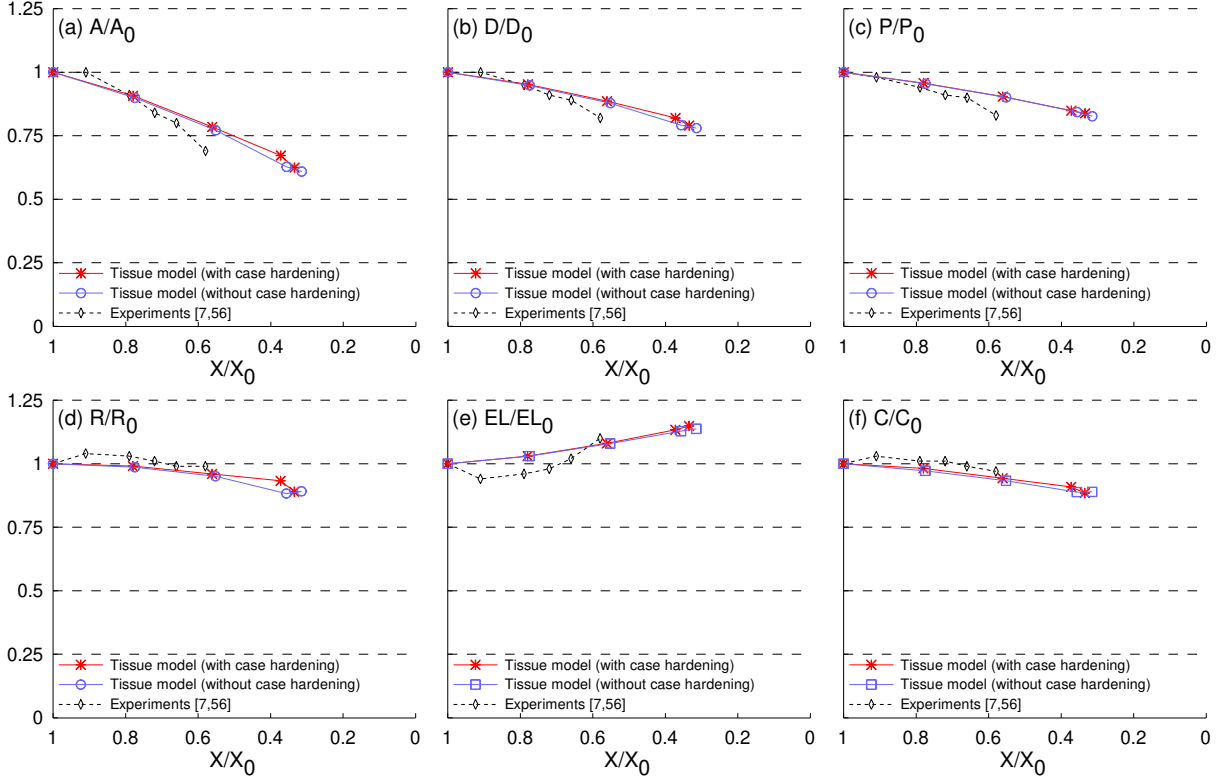
Fig. 24. Influence of case hardening for cellular geometrical parameter variations of grape tissue during drying: (a) A/A_0, (b) D/D_0, (c) P/P_0, (d) R/R_0, (e) EL/EL_0, and (f) C/C_0. (X/X_0 represents the overall average of the normalised moisture content, considering all the cells in the tissue)

8. Appendix A

8.1. Single cell model: DEM-based cell wall model

As introduced in Section 2.1, the total force ($\boldsymbol{F_k}$) on any wall particle k can be derived as:

$$\boldsymbol{F}_k = \boldsymbol{F}_{kj}^e + \boldsymbol{F}_{kj}^d + \boldsymbol{F}_{ki}^{rf} + \boldsymbol{F}_{kl}^{rw} + \boldsymbol{F}_{ki}^a + \boldsymbol{F}_{kj}^b + \boldsymbol{F}_{kj}^c. \tag{A.1}$$

Here, the $\boldsymbol{F}^e$ forces represent the cell wall resistance on extensions or contractions due to internal or external force interactions. Considering each wall element, a spring model is used to define the stiff forces $\boldsymbol{F}_{kj}^e$ on any wall particle k due to any bonded wall particle j as [35]:

$$\boldsymbol{F}_{kj}^e = GZ_0T_0\left(\lambda_\theta - \frac{1}{\alpha^2\lambda_\theta^5}\right), \tag{A.2}$$

where, G is the shear modulus ($\approx E/3$) with E being the Young's modulus of the wall material, Z_0 is the initial cell height, T_0 is the initial cell wall thickness, $\lambda_\theta = L/L_0$ is the extension ratio of any cell wall element at the current time step, L is the width of the wall element at the current time step

(distance between particle k and j) and L_0 is its initial un-deformed width. The parameter α is calculated with $\beta = 0.5$ for cylindrical cells as follows [35]:

$$\alpha = \sqrt{\frac{\beta + \sqrt{\beta^2 - 4(\beta - 1)/\lambda_\theta^6}}{2}} . \tag{A.3}$$

In Eq. A.1, $\boldsymbol{F}^d$ forces represent the viscous behaviour of the fibrous cell wall boundary and are defined by using a linear dashpot model. Therefore the viscous forces $\boldsymbol{F}^d_{kj}$ acting on any wall particle k due to the neighbouring wall particles j are calculated as [35]:

$$\boldsymbol{F}^d_{kj} = - \gamma \, \boldsymbol{v}_{kj} , \tag{A.4}$$

where, γ is the cell wall damping constant and $\boldsymbol{v}_{kj}$ is the velocity of particle k relative to particle j. The $\boldsymbol{F}^{rf}$, $\boldsymbol{F}^{rw}$ and $\boldsymbol{F}^a$ forces in Eq. (A.1) were used to define the wall-fluid interactions and boundary conditions. The repulsion forces $\boldsymbol{F}^{rf}_{ki}$ on any wall particle k from any other fluid particle i are defined as [22, 35]:

$$\boldsymbol{F}^{rf}_{ki} = f^{rf}_{ki} \, \boldsymbol{x}_{ki} , \tag{A.5}$$

where, f^{rf}_{ki} is the magnitude of the repulsion force and $\boldsymbol{x}_{ki}$ is the position vector of particle k relative to particle i. The f^{rf}_{ki} is defined according to Lenard-Jones (LJ) force type as [35]:

$$f^{rf}_{ki} = \begin{cases} f^{rf}_0 \left[\left(\dfrac{r_0}{r_{ki}} \right)^8 - \left(\dfrac{r_0}{r_{ki}} \right)^4 \right] \left(\dfrac{1}{r_{ki}^2} \right) & \left(\dfrac{r_0}{r_{ki}} \right) \geq 1 \\[3mm] 0 & \left(\dfrac{r_0}{r_{ki}} \right) < 1 , \end{cases} \tag{A.6}$$

where, r_0 is the initial gap between the two particles, r_{ki} is the current gap between them and f^{rf}_0 is the strength of the LJ contact. Furthermore, in Eq. A.1, in order to avoid unphysical self-penetrations of the non-bonded wall-wall particles, a similar force interaction was used to define the repulsion forces $\boldsymbol{F}^{rw}_{kl}$ with an LJ contact strength of f^{rw}_0. Also, the attraction forces $\boldsymbol{F}^a_{ki}$ were used to maintain fluid-wall contact during drying. Both interactions were modelled using LJ interactions with corresponding LJ contact strengths.

In Eq. A.1, a bending stiffness term ($\boldsymbol{F}^b_{kj}$) was used in order to account for the resistance that plant cell walls create when they experience local bending and wrinkling, and it was defined on any wall particle k within the k and j particle pair as [38]:

$$F_{kj}^b = \frac{k_b}{L} tan\left(\frac{\Delta\theta}{2}\right),$$ (A.7)

where, k_b is the cell wall bending stiffness, L is the width of any given wall element at any given time step, θ is the external angle between the particular wall element and the adjacent wall element as shown in Fig. 2, and $\Delta\theta$ is the change of the θ angle during time evolution. Next, as given in Eq. A.1, in order to account for cell wall contractions during drying, cell wall contraction forces (F^c) were used in the model and are defined as [37]:

$$F_{kj}^c = k_{wc}\left[L - L_0'\left[1 - \frac{a}{b}\left(1 - \frac{X}{X_0}\right)\right]\right],$$ (A.8)

where, k_{wc} is the force coefficient of wall contractions, L is the current width of any particular wall element (see Fig. 1(d)), L_0' is the width of the wall element at fully turgid condition, a and b are empirical factors, and X/X_0 is the normalised moisture content of the dried cell to be simulated. The a and b were set by considering the normalised cell perimeter trends and the same k_{wc} was used for all food materials here [37]. Further, the cell wall drying effects were accounted by proportionally reducing the cell wall mass during drying [37].

8.2. Single cell model: SPH-based cell fluid model

The resultant force F_i on any fluid particle i was defined as:

$$F_i = F_{ii'}^p + F_{ii'}^v + F_{ik}^{rw} + F_{ik}^a.$$ (A.9)

In Eq. (A.9), the pressure forces ($F_{ii'}^p$) and viscous forces ($F_{ii'}^v$) on any given fluid particle i are defined using the generic SPH fundamental formulations by involving the properties of the neighbouring fluid particles i' as [35]:

$$F_{ii'}^p = -m_i \sum_{i'} m_{i'}\left(\frac{P_i}{\rho_i^2} + \frac{P_{i'}}{\rho_{i'}^2}\right)\left(\frac{1}{Z}\right)\nabla_i W_{ii'},$$ (A.10)

$$F_{ii'}^v = m_i \sum_{i'} \frac{m_{i'}(\mu_i + \mu_{i'})v_{ii'}}{\rho_i\rho_{i'}}\left(\frac{1}{Z}\right)\left(\frac{1}{r_{ii'}}\frac{\partial W_{ii'}}{\partial r_{ii'}}\right),$$ (A.11)

where at any given time, m, P, ρ, μ, Z and W are the particle mass, pressure, density, dynamic viscosity, cell height and the smoothing kernel. For the smoothing kernel W, the quartic smoothing kernel was used for higher accuracy and stability rather than the commonly used cubic spline kernel [39]. When evaluating the W, the smoothing length was evolved in order to maintain approximately 20 particles within the influencing domain [38] :

$$h = \left(\frac{D}{D_0}\right)h_0 \,, \tag{A.12}$$

where, D is the average cell Feret diameter at the current time step, D_0 is the initial cell diameter and h_0 is the initial smoothing length (see Table 1 and Table 2). As the system evolves with time, the following equation is used to update the fluid particle pressure as a function of slight fluid density variation [22, 35]:

$$P_i = P_T + K\left[\left(\frac{\rho_i}{\rho_0}\right)^7 - 1\right], \tag{A.13}$$

where, P_T is the uniquely set initial cell turgor pressure for each of the dried cell simulations (see Section 2.4.), K is the fluid compression modulus, ρ_i is the current density of each fluid particle, and ρ_0 is its initial density assumed to be equal to the density of water. Here, the K needs to be set sufficiently higher, in order to ensure the fluid behaves in a fairly incompressible manner within the SPH scheme by minimising large density fluctuations. Next, the density of any fluid particle i is evolved using the following equation [35]:

$$\frac{d\rho_i}{dt} = \frac{1}{Z}\frac{d\rho_i^*}{dt} - \frac{\rho_i^*}{Z^2}\frac{dZ}{dt} + \frac{\rho_i}{m_i}\frac{dm_i}{dt}\,. \tag{A.14}$$

The first term in Eq. (A.14) accounts for slight density changes of the cell fluid as the cell deforms in the XY plane and ρ_i^* is the 2-D density of any fluid particle i defined as $\rho_i^* = Z\rho_i$. Then the ρ_i^* fluctuations are defined using the standard SPH continuity equation as:

$$\frac{d\rho_i^*}{dt} = m_i \sum_{i'} \boldsymbol{v}_{ii'} \cdot \nabla_i W_{ii'}\,. \tag{A.15}$$

The second term in Eq. (A.14) adds a correction to the density evolution by compensating for any cell height changes, and is defined as:

$$\frac{dZ}{dt} = \frac{Z_{t+\Delta t} - Z_t}{\Delta t}, \tag{A.16}$$

where, at any given time, $Z_{t+\Delta t}$ and Z_t are the cell heights at the current and previous time steps, and Δt is the time step size. Here, the cell height is time evolved by considering the incompressibility of the cell wall material as [35]:

$$Z = (\alpha\lambda_\theta)Z_0\,. \tag{A.17}$$

The third term in Eq. (A.14) accounts for the slight density changes within the SPH scheme as a result of the cell fluid mass transfer through the semi-permeable cell wall whenever there is a scalar difference between the cell fluid osmotic potential and the turgor pressure, and is defined as [35, 59]:

$$\frac{dm_i}{dt} = -\frac{A_c L_p \rho_i}{n_f}(P_i + \Pi)\,, \tag{A.18}$$

where A_c, L_p, n_f and Π represent total surface area of the cylindrical cell at any given time, cell wall permeability assumed to be uniform all over the cell surface, total number of fluid particles used to model the cell fluid and the osmotic potential of the cell fluid at a given dried cell state, respectively. The latter is carefully set to control the cell turgor pressure [13] because the amount of fluid transferred across the cell wall ceases when the value of P_i (> 0) becomes equal to the scalar value of Π.

The final two terms in Eq. (A.9) represent the fluid-wall boundary treatment which involves repulsion forces $\boldsymbol{F}_{ik}^{rw}$ and attraction forces $\boldsymbol{F}_{ik}^{a}$, and are defined in the same LJ force type as:

$$\boldsymbol{F}_{ik}^{rw} = \sum_{k} f_{ik}^{rw} \boldsymbol{x}_{ik} \,, \tag{A.19}$$

$$\boldsymbol{F}_{ik}^{a} = \sum_{k} f_{ik}^{a} \boldsymbol{x}_{ik} \,. \tag{A.20}$$

8.3. Tissue model

The pectin layer stiff force was defined as a linear spring model acting between the initially adjacent cell wall particles of any two adjacent cells, and defined as[25]:

$$\boldsymbol{F}_{km}^{e\_pectin} = -k_{pectin} \Delta \boldsymbol{x}_{km} \,, \tag{A.21}$$

where k_{pectin} is the pectin layer stiffness and $\Delta \boldsymbol{x}_{km}$ is the gap difference of the two particles compared to their initial gap. This force helps to maintain the gap between the wall particle pair equal to the initially set pectin layer thickness. Further, this is the only force acting in between cells if they try to separate each other beyond the initial pectin layer gap.

In case where the interacting cells become closer, pectin stiffness creates a repulsion force in order to separate the cells and thereby tries to return them to their initial relative positions. The intensity of this force is usually insufficient to fully prevent the cells from becoming very close and eventually interpenetrated. Therefore, an LJ type force is used for this purpose, and is defined as [25]:

$$\boldsymbol{F}_{km}^{rc} = \sum_{j} f_{km}^{rc} \boldsymbol{x}_{km} \,, \tag{A.22}$$

where, f_{km}^{rc} is the strength of the LJ force field and $\boldsymbol{x}_{km}$ is the position vector of particle k relative to particle m. Here, the f_{km}^{rc} is defined as similar to that of the cell wall LJ force field.

9. Nomenclature

A	cell top surface area (m^2)
A_0	cell top surface area at fresh condition (m^2)
A/A_0	normalised cell area
A_c	total surface area of the cylindrical cell (m^2)
C	cell compactness
C_0	cell compactness at fresh condition
C/C_0	normalised cell compactness
D	cell Feret diameter (m)
D_{major}	cell major axis length (m)
D_{minor}	cell minor axis length (m)
D_0	cell Feret diameter at fresh condition (m)
D/D_0	normalised cell Feret diameter
E	Young's modulus of the cell wall material (MPa)
EL	cell elongation
EL_0	cell elongation at fresh condition
EL/EL_0	normalised cell elongation
$\boldsymbol{F}^e$	cell wall stiff forces (N)
$\boldsymbol{F}^d$	cell wall damping forces (N)
$\boldsymbol{F}^{rf}$	wall-fluid repulsion forces (N)
$\boldsymbol{F}^{rw}$	wall-wall repulsion forces (N)
$\boldsymbol{F}^a$	wall-fluid attraction forces (N)
$\boldsymbol{F}^b$	forces due to the bending stiffness of the wall (N)
$\boldsymbol{F}^p$	cell fluid pressure forces (N)
$\boldsymbol{F}^v$	cell fluid viscous forces (N)
G	shear modulus of the cell wall material (MPa)
K	cell fluid compression modulus (MPa)
L	width of a given discrete wall element (m)
L'	width of a given discrete wall element at fully turgid state (m)
L_0	Initial width of a given discrete wall element (m)
L_p	cell wall permeability (m^2 N^{-1} s)

P	cell perimeter (m)
P_0	cell perimeter at fresh condition (m)
P/P_0	normalised cell perimeter
P_a	pressure of any fluid particle a (Pa)
P_T	initial cell turgor pressure (Pa)
R	cell roundness
R_0	cell roundness at fresh condition
R/R_0	normalised cell roundness
S	ratio between fluid inter-particle distance and smoothing length (r_{ab}/h)
T	cell wall thickness (m)
T_0	initial cell wall thickness (m)
TP	positive cell turgor pressure effects
W	smoothing kernel
WD	cell wall contraction effects
WC	cell wall drying effects
X	x - coordinate axis
X	dry basis moisture content (kg $_{water}$/kg $_{dry\ solid}$)
X_0	dry basis moisture content at fresh condition
X/X_0	dry basis normalised moisture content
Y	y - coordinate axis
Z	cell height (m)
Z	z - coordinate axis
Z_0	initial cell height (m)
Z_t	cell height at the previous time step (m)
$Z_{t+\Delta t}$	cell height at the current time step (m)
f_0^{rf}	strength of the LJ repulsion forces between fluid and wall particles (N m^{-1})
f_0^{rw}	strength of the LJ repulsion forces between non-bonded wall particles (N m^{-1})
f_0^{a}	strength of the LJ attraction forces between fluid and wall particles (N m^{-1})
h	smoothing length (m)
h_0	initial smoothing length (m)
k_b	bending stiffness of cell wall material (N m rad^{-1})
k_{wc}	force coefficient of cell wall contractions (N m^{-1})
m_a	mass of any particle a (kg)
n_f	cell fluid particle number
n_w	cell wall particle number
r	cell radius (m)
r_{ab}	distance between any given particle a and b (m)
t	time (s)
$\boldsymbol{v}_{ab}$	velocity of any given particle a relative to any other particle b (m s^{-1})

x_{ab}	position vector of any given particle a relative to any other particle b (m)
Δt	time step (s)
x_0	initial fluid grid spacing (m)
$\Delta \theta$	change of external angle θ of any given wall element (rad)
Δx_{ab}	change of gap difference of any two particles a and b compared to their initial gap (m)
Π	osmotic potential of the cell (Pa)
α	factor governing the relationship between z-directional extension ratio and λ_θ of any wall element
β	parameter that relates 2-D deformations to 3-D deformations of any wall element
γ	cell wall damping constant (N m^{-1} s)
ε_0	initial minimum allowed gap between outer most fluid particles and cell wall partiles (m)
θ	external angle between any adjacent cell wall elements (rad)
λ_θ	extension ratio of any given cell wall element
μ_a	dynamic viscosity of any fluid particle a (Pa s)
ρ_a	density of any given fluid particle a (kg m^{-3})
ρ_0	initial density of the cell fluid (kg m^{-3})
ρ_a^*	2-D density of any given particle a ($\rho_a^* = Z\rho_a$) (kg m^{-2})